Chapter 11

Satellite-Based Irradiance and Power Forecasting for the German Energy Market

Jan Kühnert, Elke Lorenz and Detlev Heinemann
Energy Meteorology Group, Institute of Physics, Oldenburg University

Chapter Outline

11.1. SOLAR ENERGY PENETRATION IN GERMANY

Forecasts of photovoltaic (PV) power are becoming more and more important because installed PV capacity is constantly increasing and PV power is expected to contribute a major share of future global energy supply. For an efficient

Solar Energy Forecasting and Resource Assessment. ISBN: 9780123971777

balancing of electricity supply and demand, and to maintain grid stability, a reliable prediction of the fluctuating resource solar irradiance is necessary. Today, PV-power forecasts are important components in grid operation and PV-power marketing. This chapter presents a PV-power prediction system applied in Germany. German installed PV capacity reached around 32 GWp at the end of 2012 (Wirth, 2013). Figure 11.1 shows the share of PV power in the overall energy supply in Germany for two example weeks, May and June 2012.

On sunny days, maximum PV-power production amounts up to 22 GW at noon, contributing more than 40% to overall electricity demand on typical weekend days (see on May 26 in Figure 11.1). This also shows the capability of PV power to compensate for the peak in power demand at noon, when control energy is especially costly. The high share of fluctuating PV power in Germany leads to a strong economic interest in PV-power predictions. According to the German Renewable Energy Sources Act (RES), transmission-system operators (TSOs) are responsible for balancing and marketing renewable-power feed-in and are obligated to integrate all available power from renewable-energy sources at any time.

Renewable energy is traded on the European Power Exchange Market (European Power Exchange), where power trading is organized in different time horizons: on the day-ahead market, power production is announced 1 d in advance, requiring 1-d-ahead forecasts with hourly resolution. An update of this announcement is applied on the day of planned power production in the so-called intraday market. Here, forecasts for the remaining day starting from the time this update is made (usually 11 CET or CEST) are needed. An additional spot market for power-production trading requires 2–3-h-ahead forecasts.

The PV-power forecasts used by TSOs have to be provided on a regional level, since current marketing of PV power is performed for entire control areas with an extent of several hundred kilometers. However, power companies are showing increasing interest in PV-power predictions for smaller regions and single-site predictions for applications such as demand-side management. Following these requirements, PV-power forecasts with different spatial and

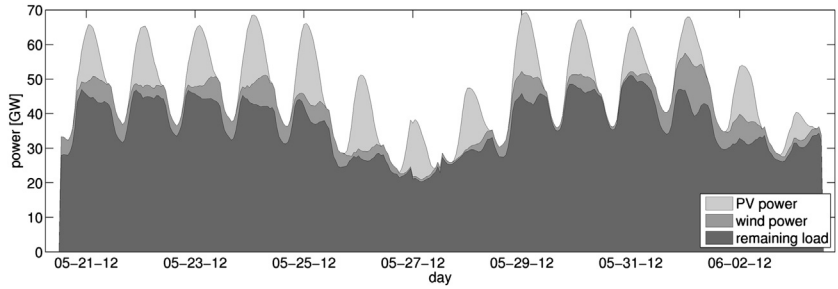

FIGURE 11.1 Contribution of solar and wind energy to total power supply in Germany for two weeks in May and June 2012 with generally high solar irradiance. The remaining load describes the contribution from conventional power plants ≥100 MW. *(Data from Energy Exchange Leipzig EEX, http://www.transparency.eex.com/de/.)*

temporal resolutions are necessary. They are based on corresponding irradiance predictions, using different irradiance forecasting methods.

Different approaches to solar-irradiance and PV-power forecasting exist (Lorenz et al., 2011; Bofinger & Heilscher, 2006; Remund et al., 2008; Bacher et al., 2009). For time horizons exceeding the current day, NWP forecasts perform best (Perez et al., 2009; Heinemann et al., 2006; Perez et al., 2011; Mathiesen & Kleissl, 2001). For forecast horizons of several hours ahead, satellite-based forecasts that detect cloud motion, as presented in this chapter, are applied (Reikard, 2009). For site-specific minute-resolved short-term forecasts, cloud detection using sky imagers is a further option (Chow et al., 2011).

In this chapter, we describe the irradiance and PV-power prediction system developed and operated by the University of Oldenburg in cooperation with Meteocontrol GmbH (Lorenz et al., 2011; Lorenz et al., 2010; Lorenz et al., 2009), which is operated for application on the German energy market. Figure 11.2 outlines the forecasting scheme: in the first step, site-specific forecasts of surface GHI are obtained from different sources, including satellite data and NWP models, and are combined with statistical postprocessing using irradiance measurements. In the following, the power output for PV plants is predicted based on predicted irradiance and plant specifications such as PV module type, tilt and orientation.

Postprocessing is applied to compare historical measured to predicted PV-power values to account for systematic deviations caused by, for example, shading of the modules in the course of the day. For regional predictions, an additional upscaling process is applied to obtain aggregate output of all systems in the corresponding area.

In this chapter, we focus on irradiance forecasts for a time horizon of some hours ahead by the detection of cloud motion based on satellite images. This forecast horizon is particularly relevant for intraday- and spot-market forecasts. Knowledge of future cloud position is the essential step in predicting irradiance for the subsequent hours. Cloud motion is detected and extrapolated using cloud-motion vectors (CMVs) derived from the most recent satellite images. This method is expected to outperform NWP forecasts up to several hours ahead (Perez et al., 2002; Lorenz & Heinemann, 2012). CMVs obtained from

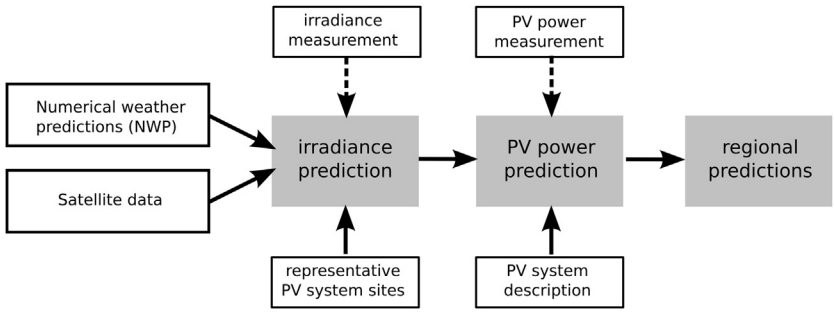

FIGURE 11.2 PV-power forecasting at the University of Oldenburg.

satellite images have been the subject of several studies, an overview of various CMV applications is given in Menzel (Menzel, 2001).

Section 11.2 is an overview of the forecasting scheme. Section 11.3 describes the satellite data and methods to derive cloud and irradiance information from satellite images. The CMV algorithm used for irradiance predictions is presented in Section 11.4, and in Section 11.5 the basic concepts of irradiance-forecast evaluation are presented. A detailed evaluation of forecast accuracy and comparison for single-station NWP forecasts, as well as for regionally averaged forecasts, in Germany follows in Section 11.6. Finally, an introduction to PV-power forecasting based on irradiance prediction is given in Section 11.7.

11.2. OVERVIEW OF THE SATELLITE FORECAST PROCESS

The variability of surface irradiance at hourly timescales is largely determined by the development of cloud structures. For many weather situations, this development is strongly influenced by the motion of existing cloud structures, which can be detected using satellite data. Images from geostationary satellites, available with high temporal and spatial resolution, are a valuable source of cloud-motion detection and are the basis for the presented forecasting method. Using Meteosat satellite data for PV-power predictions based on CMVs was first proposed by Beyer et al., (Beyer et al., 1996) and further developed by Hammer et al (Hammer et al., 1999) and Lorenz et al (Lorenz et al., 2004). In this chapter, we present and evaluate the method for irradiance forecasting based on CMVs according to Lorenz et al (Lorenz et al., 2004) (Figure 11.3).

Based on images provided by MSG satellites, information on cloud structures is derived using the semi-empirical Heliosat method (Hammer et al.,

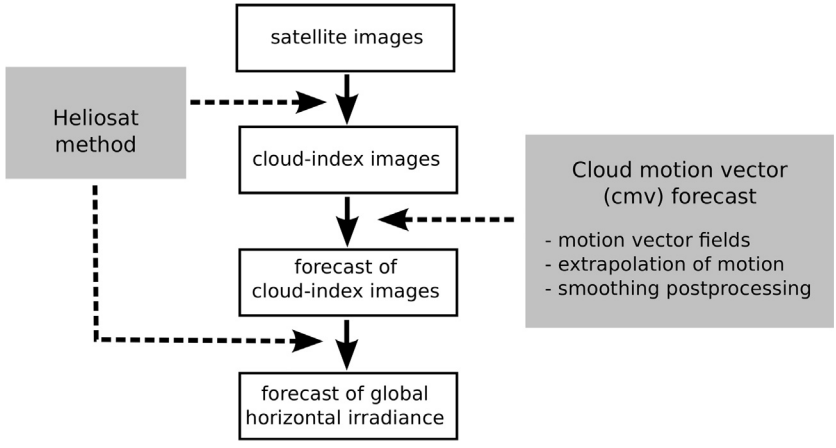

FIGURE 11.3 Forecasting scheme for GHI using CMV. Cloud-index images are calculated from Meteosat images using the Heliosat method. CMVs are applied to predict future cloud-index images, which are converted into irradiance predictions.

2003). Cloud-index images are calculated in near real time, containing information on the clouds' spatial distribution and transmissivity, providing the basis for calculation of CMVs and derivation of GHI. Cloud speed and direction (CMVs) are determined by comparing the most recent consecutive images. The extrapolation of cloud movement by applying these motion vectors to the latest satellite images leads to forecasts of future cloud-index images, optimized by a smoothing postprocessing. Forecasts of site-specific GHI are then derived from these predicted images using the Heliosat method.

11.3. IRRADIANCE FROM SATELLITE DATA

11.3.1. Meteosat Satellite

Global surface-irradiance information is gained from Meteosat satellite images operated by the European Organisation for the Exploitation of Meteorological Satellites (EUMETSAT). MSG satellites, operating since 2004, are geostationary satellites positioned in orbit at 0° longitude and latitude, placing Europe, Africa, and the Atlantic Ocean, as well as parts of Asia and South America, in their field of view. The main objective of the MSG mission is to provide data for meteorological applications in fore- and nowcasting as well as for climate research and monitoring. Data close to real time are available, providing information on the emitted and reflected irradiance from the Earth's surface and atmosphere for 11 spectral bands (long-wavelength infrared to visible) with a spatial resolution of 3×3 km. In addition, a high-resolution channel provides visible broadband irradiance (600–900 nm) with a resolution of 1×1 km at the subsatellite point, but is restricted to an area covering Europe and Eastern Africa (Schmetz et al., 2002). When using MSG images for other than subsatellite pixels, the lower and nonuniform resolutions of image pixels according to their longitude and latitude have to be considered. For example, for sites in Germany the size of one image pixel corresponds to approximately 1.2 km in the east–west direction and 1.8 km in the north–south direction.

For the cloud-motion tracking described in this chapter, the high-resolution visible-range channel (HRV) is used. MSG image-generating instruments perform a complete line-by-line scan of the Earth's disk every 15 min with a 10-bit resolution. Postprocessing carried out by EUMETSAT ensures the quality of the generated images, including completeness, geometric consistency, and radiometric calibration (EUMETSAT).

11.3.2. Heliosat Method

Global irradiance incident on the Earth's surface is determined from MSG satellite images using the Heliosat method. This method, first published by Cano et al., (Cano et al., 1986) and further developed and improved for solar energy applications by Beyer et al., (Beyer et al., 1996) and Hammer et al., (Hammer

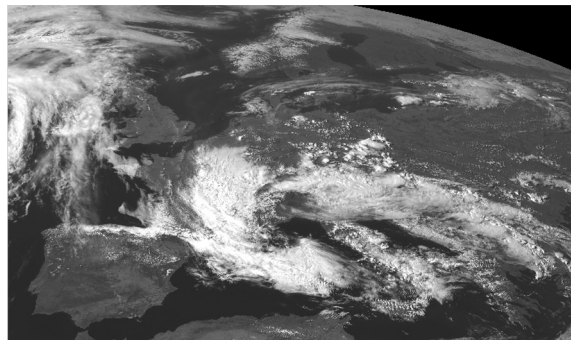

FIGURE 11.4 Example image of MSG's HRV section showing Europe, May 22, 2012, 3 PM UTC *(Image from MSG.)*

et al., 2003), uses the backscattered irradiance measured by the satellite to obtain cloud information. The intensity of reflected irradiance from clouds is higher than the irradiance intensity reflected by land and water (see Figure 11.4), except for snow-covered land areas. Therefore, in the visible spectral range, the solar irradiance backscattered by the Earth's surface and by clouds is proportional to the total cloud cover. Based on this cloud information, the transmission of radiation through the atmosphere and the resulting global surface irradiance can be derived. The following processing steps are applied. Intensity information from satellite images (i.e., the number of digital counts c for each image pixel reduced by a constant value c_0 to account for the sensor offset and normalized by the solar-zenith angle (SZA) θ_Z) is used to derive a reflectivity

$$\rho = \frac{(c - c_0)}{(\cos(\theta_Z))} \tag{11.1}$$

The reflection of an individual pixel is assumed to be emanating from ground-surface ρ_{gr} and from clouds ρ_{cl}:

$$\rho = n\rho_{cl} + (1 - n)\rho_{gr} \tag{11.2}$$

The dimensionless cloud index, n, contains information on cloud cover and transmissivity for each pixel and can be calculated using equation 11.2. Ground ρ_{gr} and cloud ρ_{cl} reflectivity are derived from sequences of satellite images. The ground reflectivity, ρ_{gr}, describes the reflectivity from ground surface and the clear atmosphere. It is a function of surface type, such as sea surface or ground with or without vegetation, seasonal changes in vegetation, and diurnal variations caused by anisotropic reflection depending on Sun elevation. Ground-reflectivity maps using the mean of the lowest reflectivity values for each pixel per time slot in the preceding 30 d create accurate and robust ρ_{gr} values. Cloud reflectivity ρ_{cl} is empirically determined by analyzing pixel-intensity histograms. These show an accumulation of points at values that represent cloudy conditions, the position in the histogram depends on Sun-satellite geometry.

Based on these points, cloud reflectivity is determined for different classes with similar geometric Sun-satellite configurations (Hammer et al., 2007). The clear-sky index k^*, defined as the ratio of global and clear-sky irradiance at the surface, gives a measure of the transmissivity of clouds and can be derived from the cloud index n with an approximately linear relationship:

$$k^* = \left\{\frac{G}{G_{\text{clear}}}\right\} \sim 1 - n \tag{11.3}$$

The clear-sky irradiance, G_{clear}, includes the dependency on atmospheric extinction by water vapor, ozone, and aerosols. Here, we use the clear-sky model by Dumortier (Dumortier, 1995) with information on atmospheric components from the Bourges (Bourges, 1992) model. Surface irradiance, G, can be derived from equation 11.3 using G_{clear} and k^* derived from satellite images.

11.4. CLOUD-MOTION VECTORS

The development of surface irradiance up to some hours ahead is strongly dependent on the movement of cloud structures, which can be detected using satellite-based methods. This section provides an overview of the processing steps necessary to derive irradiance forecasts on short-term timescales based on cloud-index images from MSG data calculated using the Heliosat method.

11.4.1. Detection of Cloud Motion

CMVs are determined by comparing consecutive cloud-index images derived from MSG HRV images. The procedure is shown in Figure 11.5. The most recent cloud-index image n_0 at time t_0 is compared with the preceding cloud-index image n_{-1} at time $t_{-1} = t_0 - \Delta t$, where Δt represents the time step between two consecutive images ($\Delta t = 15$ min for MSG images). Deriving cloud movement by comparing cloud structures in images n_0 and n_{-1} is performed by assuming (1) constant pixel intensities for cloud structures in both images and (2) smooth wind fields, which usually exist at cloud heights. These assumptions allow for detecting cloud motion by matching the same cloud pattern in consecutive images (Figure 11.6).

Rectangular areas (target areas in Figure 11.6) in image n_{-1} around the origin of each motion vector (vector grid points) are compared to equally sized areas within their neighborhood (search area) to detect the advection of cloud patterns between these images (Figure 11.6).

The detection of cloud patterns from image n_{-1} in the subsequent image n_0 is performed by minimizing the mean square pixel differences for these target areas, defined as

$$\text{MSE} = \left\{\frac{1}{N}\right\} \sum_{i=1}^{N} \left(n_0(x_i + d) - n_{-1}(x_i)\right)^2 \tag{11.4}$$

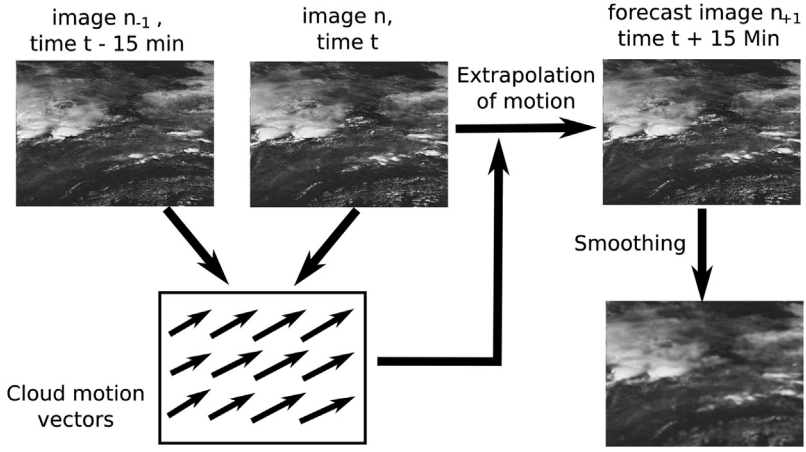

FIGURE 11.5 Procedure for cloud-index image forecasts consisting of (1) detection of motion for existing cloud structures to evaluate the most recent cloud-index images; (2) application of the derived motion-vector field to the most recent cloud-index image to extrapolate the movement of cloud structures for the next hours; (3) smoothing procedure to reduce inaccuracies in the irradiance forecasts.

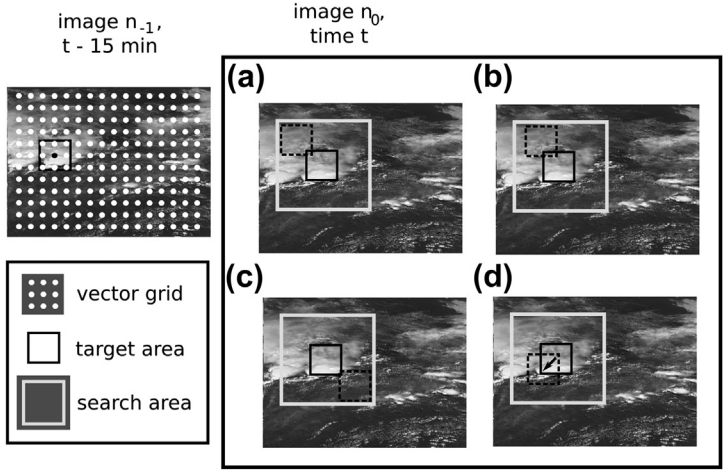

FIGURE 11.6 Scheme to detect cloud motion and vector grid, target area, and search area for calculating CMVs. For each grid point, the cloud pattern in the target area of cloud-index image n_{-1} around this point is searched for in the cloud-index image n_0. For all target areas within the search area, the MSE is determined successively (a–c). The target area identified by the minimal MSE then defines the direction and length of the motion vector (d).

where d is the shift vector of all pixels x_i in the respective area. For each part of the search area, the MSE is calculated; the target area with minimal error is selected and defines the area's motion vector. A more complex statistical method for the determination of CMV fields was also evaluated

(Hammer et al., 1999). A Monte Carlo algorithm determines the probability of a transition between images through each possible motion-vector field, and it selects the most probable CMV for a cloud-motion forecast. The evaluation of this computationally demanding model showed no significant improvement regarding its applicability and resulting forecast accuracy.

11.4.2. Determination of Model Parameters

The accuracy of CMVs in predicting future cloud-index images depends on the chosen areas used for detecting cloud patterns. Here, three different parameters can be adapted (Figure 11.6):

- distance g between two vector grid points, defining the mesh size of the grid.
- size of the target area T in which cloud patterns are compared.
- size of the search area S in image n_0 within which the target area must be detected.

These parameters were selected by minimizing RMSE forecast errors between the predicted and the original cloud-index images (Engel, 2006). Here, cloud-index images for a time period of $\sim$21 days in June 2004 were used to determine the optimized parameter set. The impact of varying parameters was tested for predicting images 1 time step $\Delta t = 15$ min ahead. According to the different pixel resolutions in the east–west and north–south directions, the vector-grid, target- and search-area sizes are defined with the ratio of 3:2 pixels for width and height to obtain an almost squared area.

The spatial resolution of the vector fields defines the distance between neighboring motion vectors and therefore the number of vectors in the image. For operational use, the grid size was chosen by optimization with respect to forecast resolution and computational cost, resulting in a vector-grid size of around 43×43 km^2.

The target area defines the rectangular section in image n_{-1}, which is compared and detected in image n_0, centered on the origin points of the vector field. By minimizing the forecast RMSE for different target-area sizes, a size of $\sim 110 \times 110$ km^2 was selected. Smaller target areas have a limited amount of available and stable cloud patterns required for matching cloud structures. On the other hand, for larger areas no significant improvement in cloud-pattern detection is observed. The larger the target area, the less valid the assumption of uniform cloud movement; rather, cloud structures move in different directions within one target area.

The maximum size of the search is determined by the maximum possible speed of cloud movement. However, evaluations showed that the best forecast results with a smaller search area (since this decreases the likelihood of mismatches) than specified by this condition, leading to a chosen search-area size corresponding to cloud speeds of 25 m/s.

TABLE 11.1 Vector-Grid, Target-Area, and Search-Area Sizes (km)

Vector grid	43 × 43
Target area	110 × 110
Search area	200 × 200

Table 11.1 provides an overview on the parameters derived for optimizing CMV forecasts.

11.4.3. Forecasting by Extrapolation of Motion

Future cloud-index images are created by applying motion vectors to the most recent image to extrapolate cloud movement. The extrapolation is carried out by segmentally moving the existing cloud structures along the vectors for this region. Assuming persistent cloud patterns and wind fields, this method allows forecasting of cloud-index images for the subsequent hours.

A motion-vector field $d(x_i)$ is applied to a cloud-index image using the same $\Delta t = 15$ min time step. Cloud-index images $n_1, n_2, \ldots n_n$ are generated, representing the forecast images $n_k = n_0 + k \cdot \Delta t$. For example, the 15 min cloud-index forecast (cloud index n_1), is derived by applying the motion vector $d(x_i)$ to cloud index n_0 via $n_1(x_i) = n_0(x_i - d(x_i))$ for each pixel x_i. That is, for each pixel in the forecast image n_1, cloud information is obtained by reverse application of the corresponding motion vector. This has the advantage that cloud information is (directly) available for all pixels and so gaps due to different cloud movements for different pixels are avoided. Cloud-index image n_i *is* extrapolated step by step: $n_0 \rightarrow n_1 \rightarrow n_2 \rightarrow \ldots \rightarrow n_i$ rather than by using a scaled motion vector to extrapolate $n_0 \rightarrow n_i$ in one step. In other words, cloud velocities at a specific location are assumed to persist in contrast to a propagation of wind speed with cloud motion. Thus, clouds may change direction and speed during their movement, according to variation in wind fields with location. The shift of the image pixels with a motion vector is performed block-wise with the resolution of the vector grid.

The extrapolation of cloud movement does not consider the formation and dissolution of clouds. Also, changes in wind speed and direction are not considered and can thus lead to increasing forecast errors with increasing forecast horizons.

11.4.4. Postprocessing: Smoothing

As a final step, the extrapolated cloud-index images are postprocessed using a smoothing filter. Postprocessing reduces the impact of inaccuracies in the

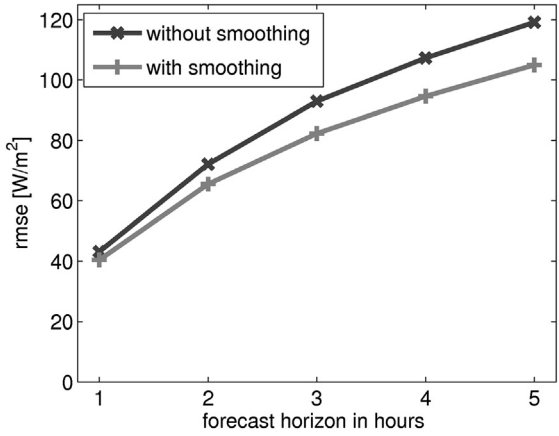

FIGURE 11.7 Comparison of RMSE using smoothed and nonsmoothed extrapolated cloud-index images dependent on the forecast horizon for a single site from July to September 2011.

extrapolated images, which mainly occur because of spatial differences between predicted and actual cloud positions. These deviations are caused by undetected changes in cloud-motion direction and speed and by propagation of fine cloud structures, which are likely reshaping during cloud movement and are therefore unpredictable. Applying a smoothing filter leads to a considerable improvement in forecast quality by reducing this noise (Lorenz & Heinemann, 2012).

Each pixel of the extrapolated image is smoothed, averaging all pixel intensities within an area of size $a \times a$ around it. Since the extrapolation of cloud structures leads to an increasing propagation of forecast errors with forecast horizon, the optimal size of the smoothing area a changes with each time step of extrapolation. For larger timescales, favoring larger forecast errors, a more extensive smoothing is favorable. The operational setting for parameter a was adapted to the forecast horizon by evaluating and minimizing the forecast error for each time step, as performed when optimizing the parameter set for deriving motion-vector fields (Engel, 2006). Figure 11.7 shows the improvement in forecast accuracy with smoothed extrapolated cloud-index images depending on forecast horizon.

11.5. EVALUATION

For irradiance forecasts serving as a basis of PV-power predictions, estimating accuracy is fundamental for integration of these predictions into energy systems. The presented CMV forecasts are validated against ground measurements and compared to other forecasting methods. In this section, overviews of the applied metrics as well as the evaluation dataset and reference forecasts are offered.

11.5.1. Evaluation Measures and Period

CMV-forecast accuracy is analyzed against (1) satellite-derived irradiance from cloud-index images actually received at the predicted point in time to evaluate the quality of cloud-index predictions, and (2) ground-measured irradiance, including error caused by conversion of cloud index to irradiance. As a statistical measure, the RMSE between measured and predicted irradiance is calculated as follows:

$$\mathrm{RMSE} = \frac{1}{\sqrt{\mathrm{N}}} \sum_{i=1}^{N} \sqrt{\left(I_{\mathrm{pred},\,i} - I_{\mathrm{meas},\,i}\right)^2} \tag{11.5}$$

with the overall number N of data points i and the predicted and measured irradiance $I_{\mathrm{pred},i}$ and $I_{\mathrm{meas},i}$. The ground irradiance, $I_{\mathrm{meas},i}$, consists of hourly mean-irradiance values from meteorological stations (Figure 11.8). Additionally, the MBE and correlation coefficient are given for part of the evaluations. (Refer to Chapter 8.) Predicted irradiances $I_{\mathrm{pred},i,\mathrm{CMV}}$ from CMV forecasts are hourly averages of 15 min samples. Relative RMSE values are given with respect to averaged irradiance.

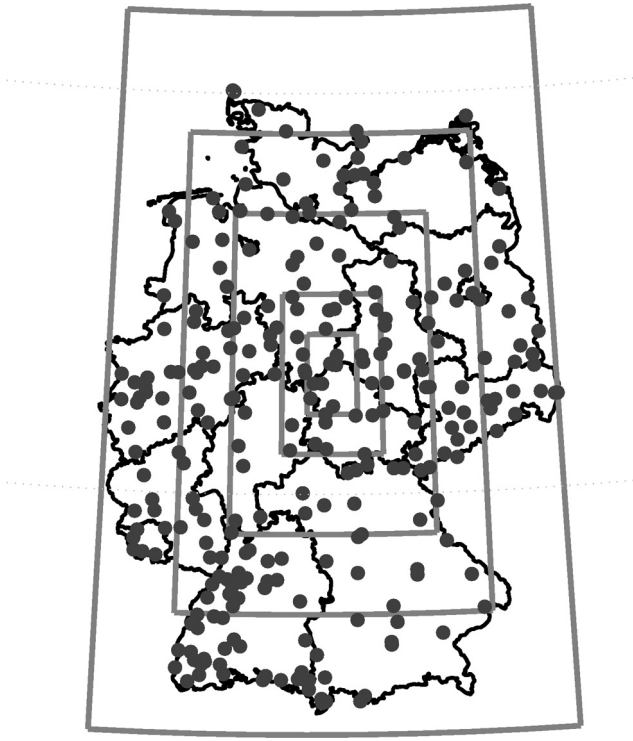

FIGURE 11.8 Meteorological stations used in the evaluation dataset and selected regions for the evaluation described in Section 11.6.2 (from single stations to all sites).

For all forecast methods and measurements, a common dataset with equal temporal resolution is used in order to maintain method comparability. Here, we select the evaluation period from July 2011 (marking the start of operational use of CMV forecasts at the University of Oldenburg) through June 2012, containing a year of data. The evaluation for all forecasts is limited to daylight values and to hours for which CMV forecasts are generated at a Sun elevation higher than 10°. The dataset used for evaluating the irradiance predictions consists of pyranometer measurements of the GHI at 274 stations in Germany operated by the German Weather Service (DWD) (Deutscher Wetterdienst) and Meteomedia GmbH (Meteomedia GmbH), distributed over Germany (Figure 11.8).

11.5.2. Reference Forecasts: ECMWF and Persistence

The forecast performance of CMVs is compared against NWP and persistence forecasts. NWP forecasts are part of the PV-power prediction system and are the standard forecasting approach in most power-prediction systems. Cloud-cover persistence represents a simple approach that works best for very short-term forecasts.

ECMWF Global Model Irradiance Forecasts

Global NWP models provided by the European Centre for Medium-Range Weather Forecasts (ECMWF) are used to derive irradiance forecasts up to 5 d ahead. These models predict the development of the atmospheric state using a parameterization of atmospheric conditions and numerically solved differential equations. For global models, a spatial and temporal discretization with a fixed resolution is used.

For this evaluation, ECMWF global model forecasts with 3 h time steps and a spatial resolution of 0.25° × 0.25° are used, computed twice a day (0000 and 1200 UTC). Forecasts from the 0000 UTC forecast run are used. Several postprocessing steps are performed in order to achieve optimization of temporal and spatial resolution for site-specific irradiance forecasts (Lorenz et al., 2009; Lorenz & Heinemann, 2012). First, a spatial averaging procedure is performed, averaging over regions of 100 × 100 km^2, leading to an increase in forecast performance as described in Lorenz et al (Lorenz et al., 2009). In a second step, temporal interpolation procedures are implemented to derive hourly irradiance values, using a linear interpolation of the clear-sky index, k^*. From 3 h mean-irradiance $I_{\mathrm{NWP,3h}}$ values, an average 3 h clear-sky index, $k^*_{3\mathrm{h}} = \left\{\frac{I_{\mathrm{NWP,\,3h}}}{I_{\mathrm{clear,\,3h}}}\right\}$, is calculated. These $k^*_{3\mathrm{h}}$ values are interpolated linearly to obtain 1-h resolved clear-sky indices $k^*_{1\mathrm{h}}$, leading to a predicted irradiance $I_{\mathrm{NWP,\,1h}} = k^*_{1\mathrm{h}} \cdot I_{\mathrm{clear,\,1h}}$. In a last step, systematic deviations in forecast accuracies as a function of

clear-sky index and solar-zenith angle are bias-corrected based on irradiance measurements of the preceeding 30 d in the considered region (Lorenz & et al., 2009).

Persistence Forecasts

Irradiance measurements I_{meas} are used to derive the clear-sky index k^*_{meas}. To obtain future irradiance values, k^*_{meas} is assumed to persist for the next hours, leading to an irradiance prediction I_{pers} that takes the daily course of irradiance into account. Hence, the predicted irradiance at time $t = t_0 + \Delta t$ is calculated as

$$I_{\text{pers},\,\Delta t}(t) = k^*_{\text{meas}}(t_0) I_{\text{clear}}(t) \tag{11.6}$$

The advantage of using ground measurements and assuming k^* persistence to validate CMV forecasts, is that inaccuracies caused by conversion of satellite images to irradiance will be revealed. The assumed persistence of cloud cover is good for very short timescales and for stable weather conditions with small changes in cloud cover.

11.6. EVALUATION OF CMV FORECASTS

In this section, we provide a detailed evaluation of forecasts based on CMVs. Forecast accuracy with respect to single sites is shown, and accuracy using regional averaged forecasts as applied to grid management is discussed. Finally, a detailed evaluation according to seasonal, daily, and weather-dependent variations is provided.

11.6.1. Single-Site Forecasts

The irradiance at a specific ground position is predicted by evaluating the extrapolated and smoothed cloud-index image at the corresponding pixel. First, we compare irradiances derived from predicted cloud-index images to irradiances derived from actual cloud-index images. Figure 11.9 shows the diurnal development of an irradiance forecast at a meteorological station in South Germany for a single day in April 2012.

In the early morning, irradiance forecasts for the day show larger deviations from the actual irradiance (derived from satellite images). The forecast matches well only a few hours ahead, showing larger deviations with growing forecast horizons and not capturing fluctuations in the later hours. In later forecast issue times, fluctuations of irradiance are also captured and show a good match to irradiance from actual cloud-index images several hours ahead. The quality of the forecast strongly depends on the forecast horizon but also depends on the weather situation. Irradiance forecasts for forecast horizons of 1 and 3 h ahead are shown for several days with different weather

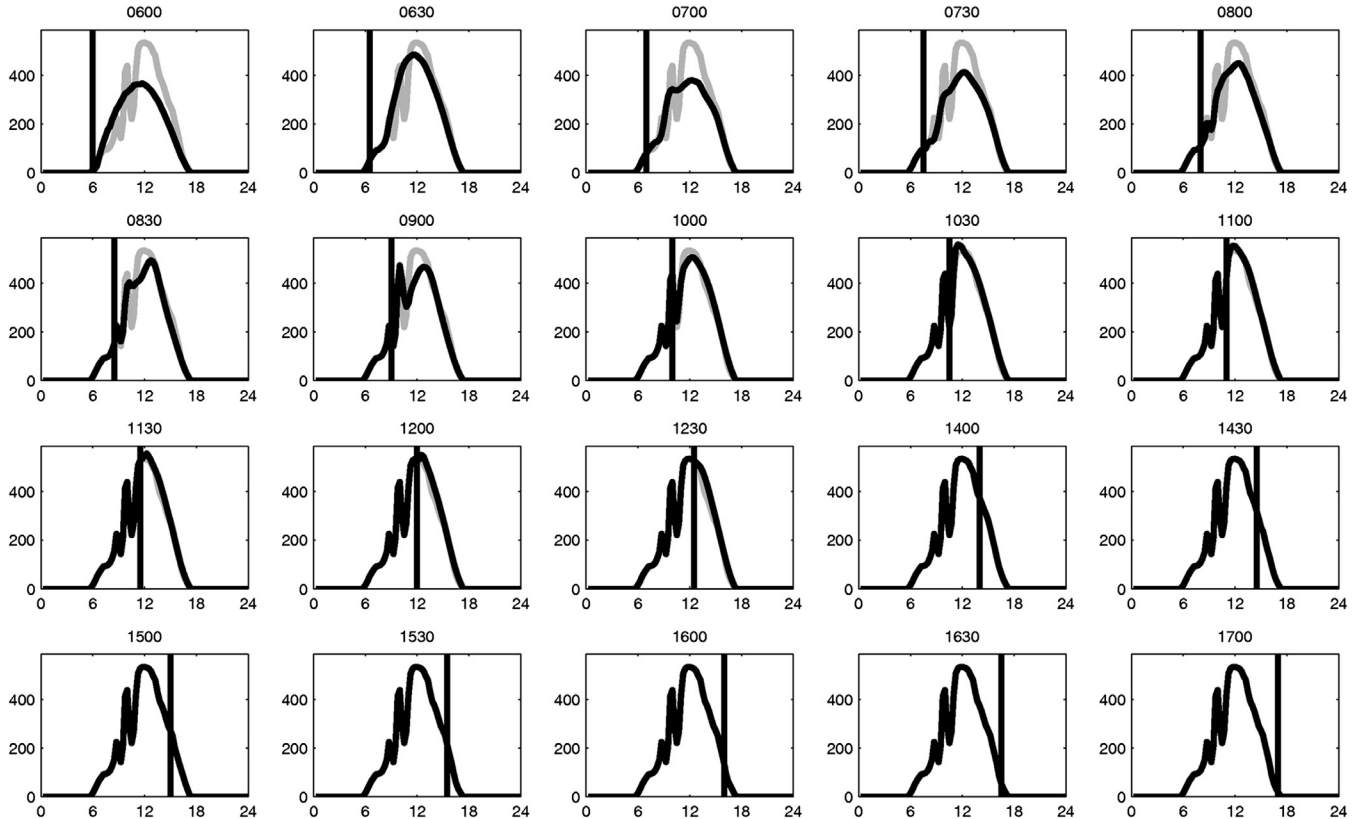

FIGURE 11.9 Series of irradiance forecasts for one day in March 2012 (*black curve*) for one example meteorological station in South Germany. The forecasts are generated at gradual time steps (15 min; here only 30 min steps are shown) from 0600 h to 1700 h (*vertical line*). Irradiance derived from satellite images at this station is shown (*gray curve*).

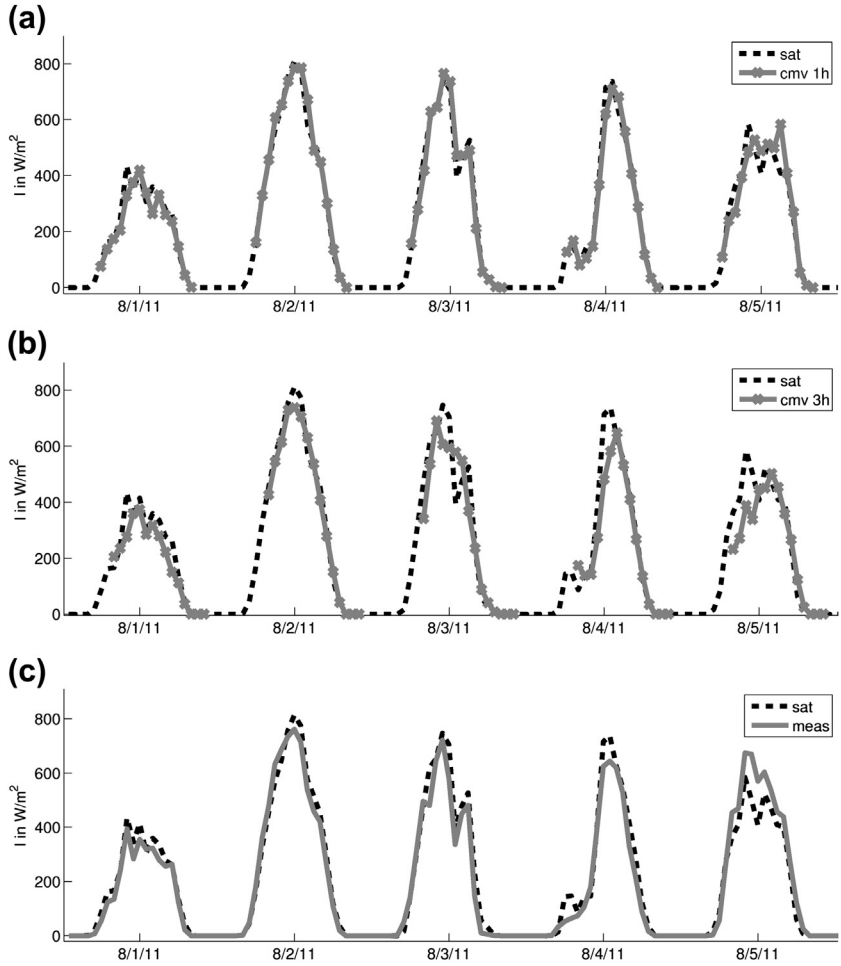

FIGURE 11.10 Comparison of CMV-predicted and satellite-derived irradiance for a 5-day period in August 2011 for a single station in South Germany. The prediction by CMV is displayed for 1 h (*top*) and 3 h (*center*) ahead, respectively. The bottom time series compares satellite-derived irradiance with ground measurements, showing the error of the satellite method, including the derivation of cloud-index images and the conversion into ground irradiance. The satellite-derived irradiance is from real (not forecasted) cloud-index images.

situations (clear-sky, cloudy and mixed) in Figure 11.10. Generally, the forecast error is much larger for 3 h ahead than for 1 h ahead on partly cloudy days, while for clear-sky days (e.g., August 2, 2011) all forecast horizons show a good match.

The comparisons given so far show deviations between forecast and satellite-derived irradiances, neglecting the inaccuracies occurring by converting the satellite images to ground irradiance. This error, resulting from

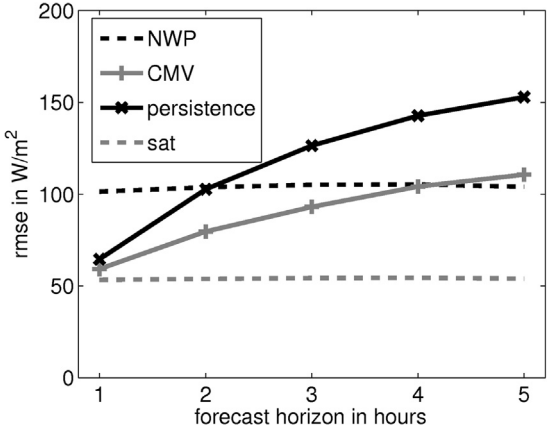

FIGURE 11.11 Root mean square error (RMSE) of CMV forecasts, NWP forecasts, and persistence forecasts as well as satellite-derived irradiance compared to ground-measured mean irradiance as a function of forecast horizon. All 274 sites of the dataset have been used for evaluation.

deriving cloud-index images and converting cloud information into ground irradiance, is shown at the bottom of Figure 11.10.

For quantitative evaluation, the RMSE of CMV forecasts is displayed for the entire dataset of all stations as a function of the forecast horizon in Figure 11.11. The reference forecasts described in Section 11.5.2 and the RMSE of the Heliosat method are also shown. The RMSE of ECMWF forecasts integrates forecast horizons up to 2 h based on the forecast run at 0000 UTC and therefore is largely independent of the forecast horizon. The slight dependencies on the forecast horizon, observed for the RMSE for ECMWF forecasts as well as for the Heliosat method, are due to the use of different datasets for each forecast horizon. These are determined by the limited availability of CMV forecasts for certain forecast horizons, since only CMV forecasts calculated for solar elevations higher than 10° are included, as further outlined in Section 11.6.3.

From Figure 11.11, the optimum forecast method for each forecast horizon can be determined. This information is helpful for optimizing irradiance- and PV-power prediction by selecting the appropriate method according to the horizon. Predictions based on the assumption of k^* persistence show good results for horizons 1 h ahead, mainly because they are based on irradiance measurements instead of satellite or NWP models. With increasing forecast horizons, accuracy markedly decreases because the assumption of persistent cloud cover is less applicable.

For a forecast horizon of 1 h, CMV forecasts are close to the lowest possible error limit represented by the satellite-to-irradiance conversion error. With forecast horizon, inaccuracies from CMV forecasts are increasing, and become equal to the ECMWF forecasts at around a 4 h horizon. For larger horizons, the NWP forecasts perform better, since cloud formation and dissolution are also considered there.

11.6.2. Regional Forecasts

For PV-power predictions on the energy market, regional forecasts are of major interest—for example, TSOs use forecasts for their control areas, which usually cover regions with scales of several hundred kilometers. Regional forecasts, derived by averaging the predicted irradiance over all stations within a region, are investigated in this section. Usually, they show higher accuracies than do single-station forecasts (Figure 11.12).

Because of spatial averaging, a general trend of decreasing forecast error with increasing region size can be observed for both NWP and CMV forecasts. Considering regional forecasts, the overall weather situation is more important than determining the exact actual cloud position, as for single-site predictions. All following evaluations of regional forecasts refer to the average of stations in Germany (rightmost column in Figure 11.12). Figure 11.13 shows regionally averaged CMV forecasts as compared with corresponding irradiance measurements as well as NWP forecasts. The forecast accuracy of CMV is greater than that of NWP forecasts for most of the days, while showing a lower accuracy for 3 h forecasts on some of the days.

Figure 11.14 shows scatter plots for 1 and 3 h forecasts versus measured irradiances for regional averages for the entire evaluation period. Forecasts up to 3 h ahead are especially relevant for spot-market trading. CMV forecasts perform significantly better than NWP forecasts, featuring less spread and less

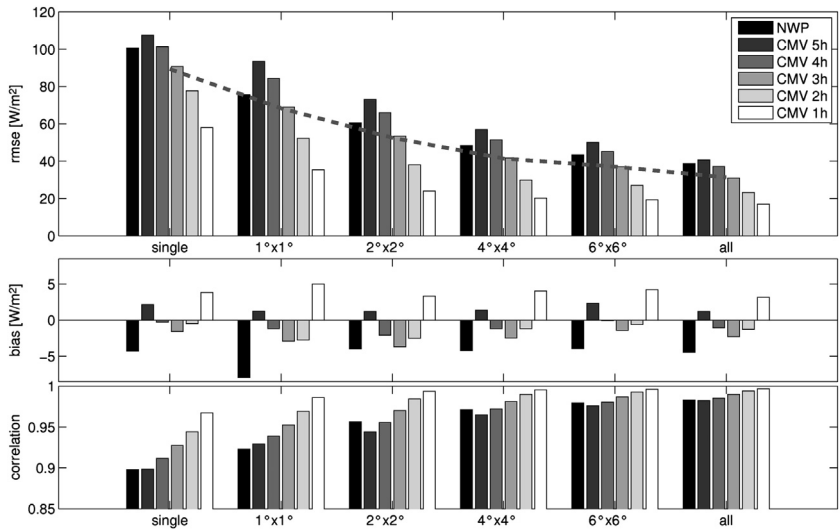

FIGURE 11.12 RMSE (*top*), bias (*center*) and correlation coefficient (*bottom*) for CMV and ECMWF-based forecasts for different region sizes, from single stations toward an average of all meteorological stations of the dataset, extending the test regions in 1° and 2° steps according to Figure 11.8.

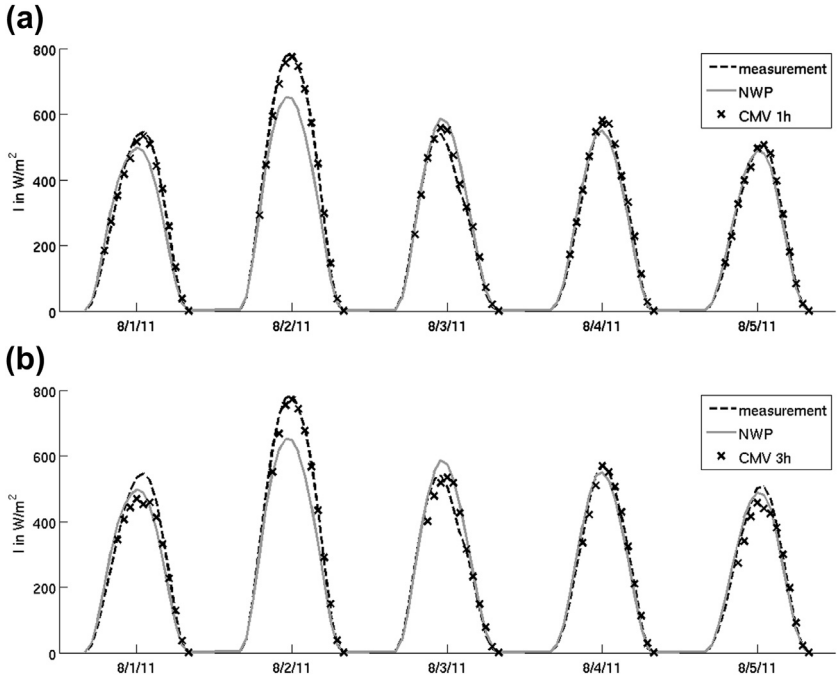

FIGURE 11.13 Time series of ground and predicted irradiance for five days in August 2011, averaged over all sites in the dataset. The CMV forecast for 1 h (*top*) and 3 h (*bottom*) horizons is compared to NWP-forecast and irradiance measurements.

systematic deviations at higher irradiance values. The RMSE of CMVs for each horizon compared to reference forecasts is shown in Figure 11.15 for regional forecasts, in analogy to Figure 11.11 for single sites. At a horizon of 1 h ahead, forecast accuracy reaches the quality of satellite-to-ground irradiance conversion, but shows slightly more errors than persistence. For 2–4 h forecast horizons, CMVs outperform both NWP and persistence forecasts.

11.6.3. Error Characterization

This section provides a more detailed characterization of error in various prediction methods as a function of different parameters.

Sun Elevation

CMV forecasts are based on deriving cloud information. The capability of reliably detecting clouds is therefore an essential prerequisite for generating them. However, when using the visible spectral channel, a proper detection of cloud position and movement is possible only above a certain Sun elevation. The decisive factor is Sun elevation at the time the forecast is generated—that

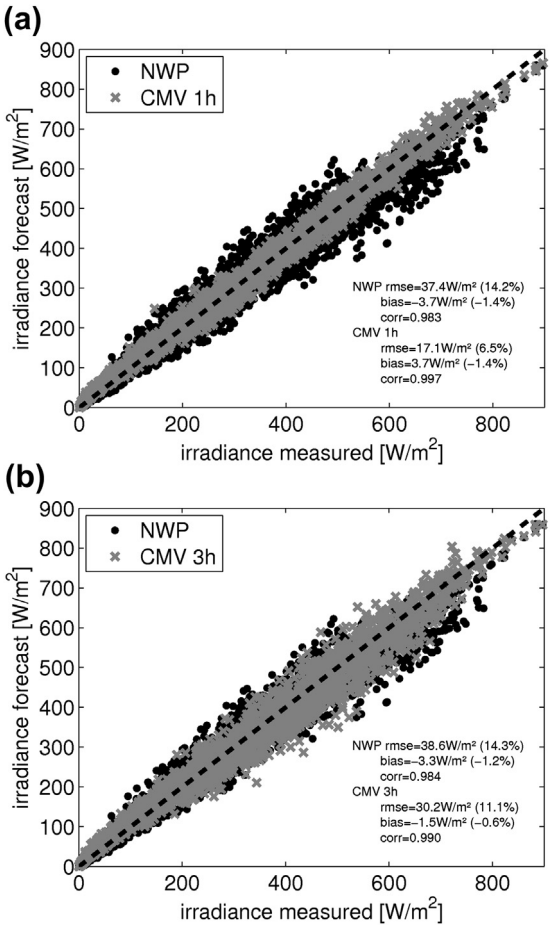

FIGURE 11.14 Scatter plot of 1 h and 3 h CMV forecasts and intraday NWP forecasts compared to ground measurements.

is, at the time the first cloud-index image for creating the CMV is derived. Figure 11.16 shows CMV and NWP forecast RMSE as function of Sun elevation. Two characteristic Sun-elevation values can be observed: that below which CMV forecast errors strongly increase (around 5°) and that where CMV forecasts become more accurate than NWP forecasts (around 15°). Figure 11.17 shows that both limits increase with forecast horizon.

Since the strong increase in forecast inaccuracy due to low Sun elevation occurs only below ∼10° for all forecast horizons, this elevation is selected as being a critical limit. As a consequence, evaluations presented in this chapter include only forecasts generated at Sun elevations above 10° in the early morning hours. Selecting a limiting Sun elevation restricts the hours a day CMV forecasts are available, especially in the winter months.

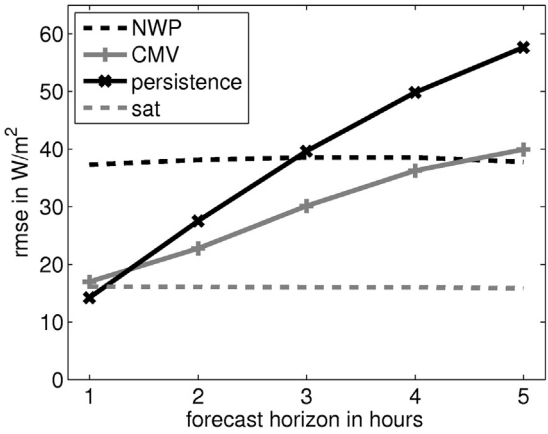

FIGURE 11.15 RMSE for regional forecasts for Germany as a function of the forecast horizon for CMV and persistence forecasts, compared to NWP intraday forecasts and satellite-derived irradiances (no forecast). The variation in NWP forecasts and satellite irradiance with forecast horizon are due to the evaluation of different datasets depending on the horizon.

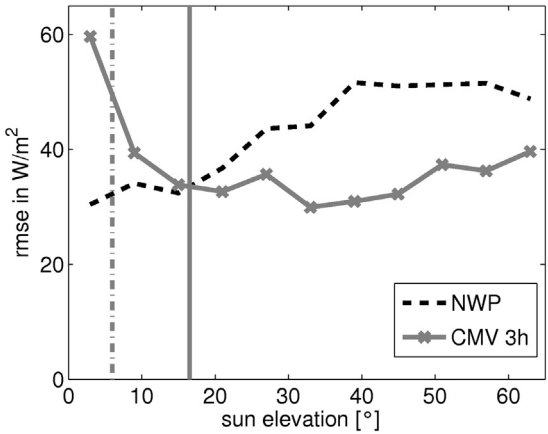

FIGURE 11.16 RMSE for 3 h CMV and NWP forecasts (averaged over all stations) as a function of Sun elevation at the time of forecast generated. *Vertical lines* mark the limits evaluated in Figure 11.17.

Daytime Dependency

Figure11.18 shows the dependency of RMSE on hour of day (in UTC) for the averaged single-site evaluation for ECMWF and CMV forecasts in July 2011. The forecast error for all methods shows a clear dependency on the daily course of irradiance because, for example, the maximum irradiance and therefore the maximum possible errors occur at noon. In addition, the figure illustrates the limited availability of CMV forecasts for different forecast horizons. This leads to different datasets depending on the forecast horizon for the evaluations shown in Figures 11.11, 11.15 and 11.21.

Dependency on the Clear-Sky Index

The quality of CMV forecasts depends on weather condtions—most significantly the clear-sky index k^* (Figure 11.19). The evaluation of single sites

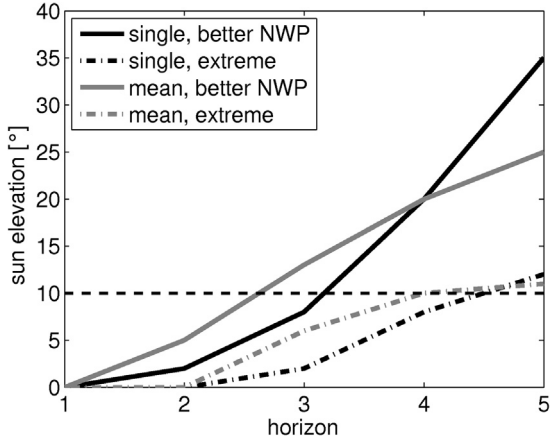

FIGURE 11.17 Forecast accuracy limits for Sun elevation as function of forecast horizon and evaluated for the average of all single sites and mean forecasts. "Better NWP" refers to the crossover between NWP and CMV (*right vertical line* in Figure 11.18) and "Extreme" refers to the elevation angle below which CMV errors increase dramatically.

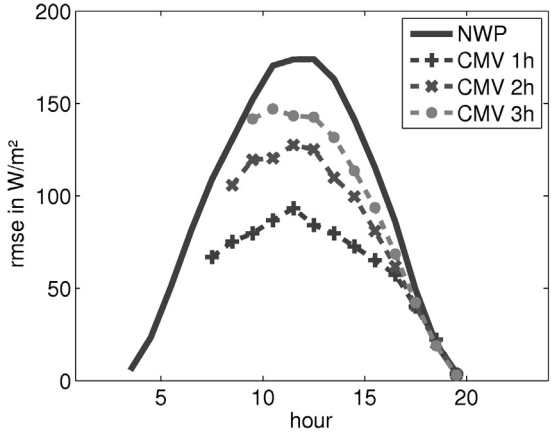

FIGURE 11.18 Irradiance-forecast error as a function of hour of day (UTC) averaged over all single sites in July 2011. The forecast error follows the daily course of irradiance.

shows that CMV accuracy strongly depends on on the clear-sky index. Overcast cloud cover and clear-sky conditions show a better predictability than conditions with broken cloud cover, where clear-sky and cloudy conditions both occur within the 1 h average. These cloud conditions often feature high spatial and temporal variability and are difficult to predict for single stations. This especially holds for persistence-based forecasts, where the impact of variable cloud conditions is even stronger than for CMV forecasts. Clear-sky and overcast situations show less fluctuation, so persistence is more accurate.

For a regional evaluation, high forecast error for broken cloud conditions does not occur, since the local variabilities are averaged out. Here, a tendency toward higher RMSE values for NWP and CMV forecasts close to clear-sky indices $k^* \approx 1$ is visible, which can at least partly be explained by larger irradiance magnitudes in clear conditions.

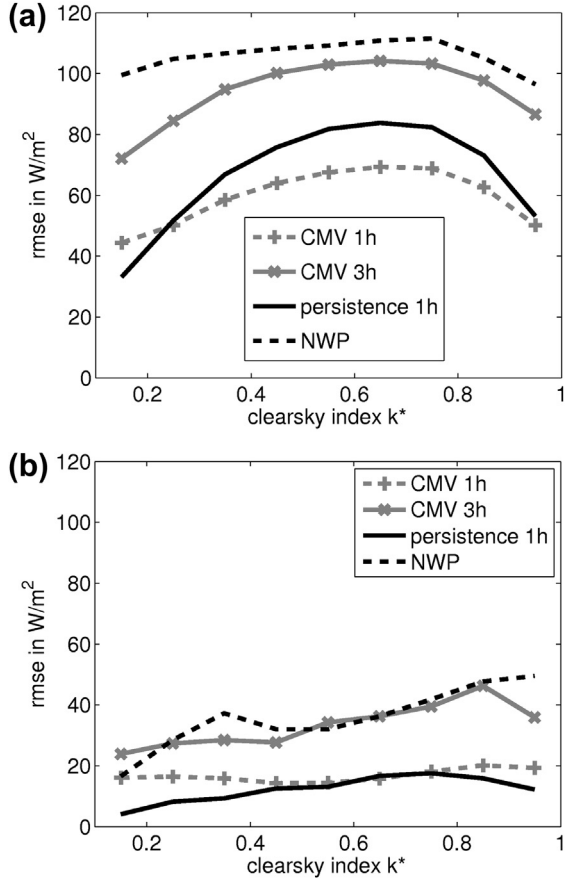

FIGURE 11.19 Dependency of CMV error (1 h and 3 h horizon), persistence error (1 h), and NWP error on clear-sky index k^* derived from ground measurements. Evaluation of single sites (*top*) and mean values (*bottom*).

Seasonal Evaluation

The quality of CMV and NWP predictions depends on the weather situation and Sun elevation. Since weather and elevations change by season, these dependencies can also influence forecast accuracy depending on month and season. Figure 11.20 shows forecast accuracy by month for NWP and CMV forecasts with a 2 h horizon in absolute and relative RMSE values for single-site and regional forecasts. The strong impact of seasonal course is visible. In winter months, the absolute error for CMV and NWP forecasts is small because of generally low irradiance. The relative RMSE in winter months, however, is much higher than in summer months for both CMV and NWP. CMV shows greater forecast accuracy than NWP except for months with very low Sun elevations: November through February.

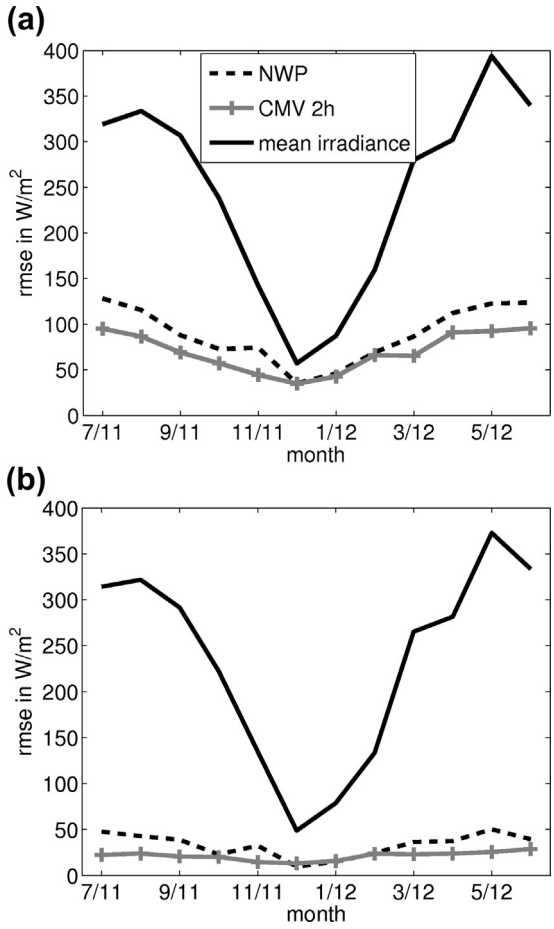

FIGURE 11.20 Comparison of CMV forecasts with 2 h horizon to NWP forecasts as a function of month (July 2011 to June 2012) for single sites *(a), (c)* and regional averages *(b), (d). a, b)* Absolute values of RMSE; *c, d)* plots showing relative RMSE (rRMSE) in percentage. rRMSE is normalized by the average monthly irradiance considering only daytime values.

An overview of forecast accuracy as a function of forecast horizon and season is given in Figure 11.21, evaluated for regional forecasts. In summer and fall, CMV performs better than persistence and ECMWF for all evaluated forecast horizons up to 5 h. For all seasons, the error of 1 h CMV forecasts is determined almost solely through satellite-to-irradiance conversion. Except for the summer months, persistence forecasts perform better for the 1 h forecast horizon. In the winter, forecast performance significantly differs from the that in other seasons. Here, CMV shows higher forecast error than NWP from 2 h onward. Persistence forecasts perform better than CMV for all forecast horizons. In spring NWP forecasts show better results than CMV forecasts for horizons larger than 3 h. This seasonal evaluation is for July 2011 through June 2012 and does not necessarily show a general trend, but outlines some seasonal

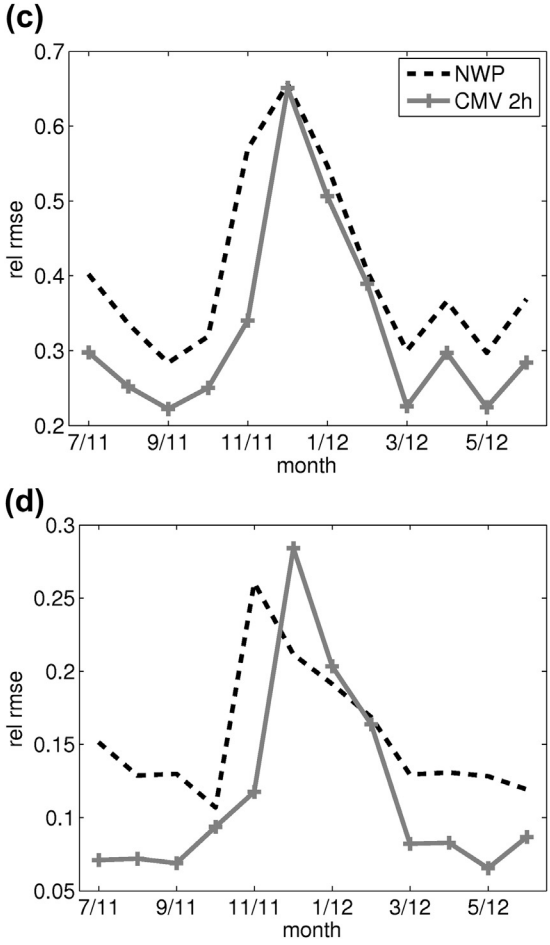

FIGURE 11.20 Continued.

factors that influence CMV forecast accuracy. For the spring months, high CMV forecast error is partially due to formation and dissolution of clouds and fog structures. Formation and dissolution are not detectable by the CMV method, which mainly aims at the detection of cloud motion. For the winter months, low Sun elevation is a major reason for CMV's poor performance.

11.7. PV-POWER FORECASTING

The aim of the presented forecasting method is to provide regional PV-power forecasts for utility applications. Therefore, the next step is predicting the output of PV systems based on GHI forecasts. Several methods exist for converting predicted irradiances to PV-power output, such as explicit physical

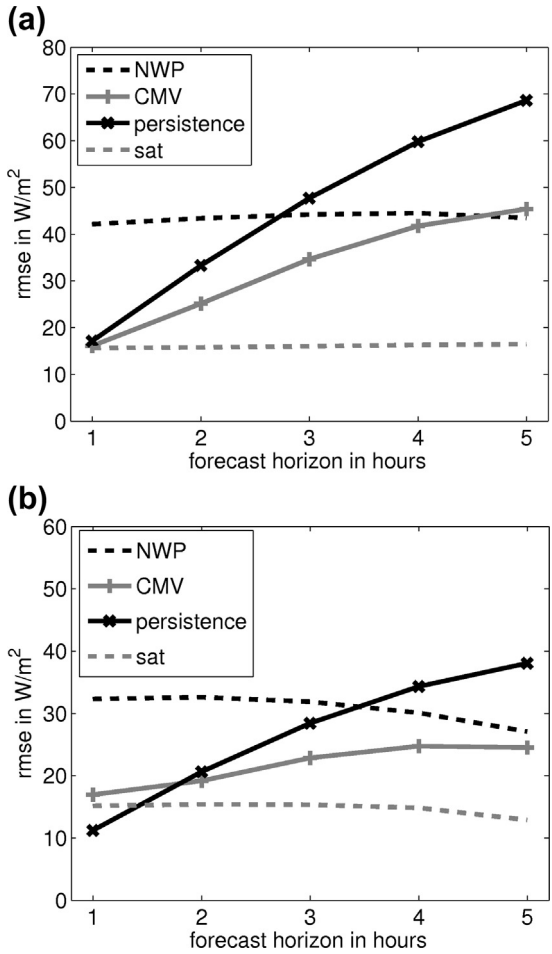

FIGURE 11.21 CMV, NWP, and persistence forecasts and satellite-derived irradiance errors as a function of forecast horizon for different seasons for regional averages of irradiance: (a) summer months (July/August 2011, June 2012); (b) fall months (September−November 2011); (c) winter months (December 2011 to February 2012); and (d) spring months (March−May 2012). The variation in NWP forecasts and satellite irradiance with forecast horizon are due to the evaluation of different datasets depending on horizon, as depicted in Section 11.6.3.

modeling of the processes involved, statistical methods correlating irradiance forecasts with PV-power measurements, and combinations of physical and statistical approaches (Lorenz & Heinemann, 2012). Here, the basic steps in deriving PV-power predictions at specific sites using physical modeling for PV systems are outlined, according to Lorenz et al (Lorenz et al., 2010).

To model the output of a PV system, information on the system and its components is required, such as module orientation and tilt, rated power, and change in efficiency with module temperature. Here, we refer to PV systems with a fixed tilt angle, representing the most common configuration in Germany. First, the predicted GHI is converted to irradiance on the module plane (e.g., Klucher et al., (Klucher, 1979)). For this conversion, the incident irradiance is split into parts arising from direct-beam and diffuse sky radiation. The diffuse and direct

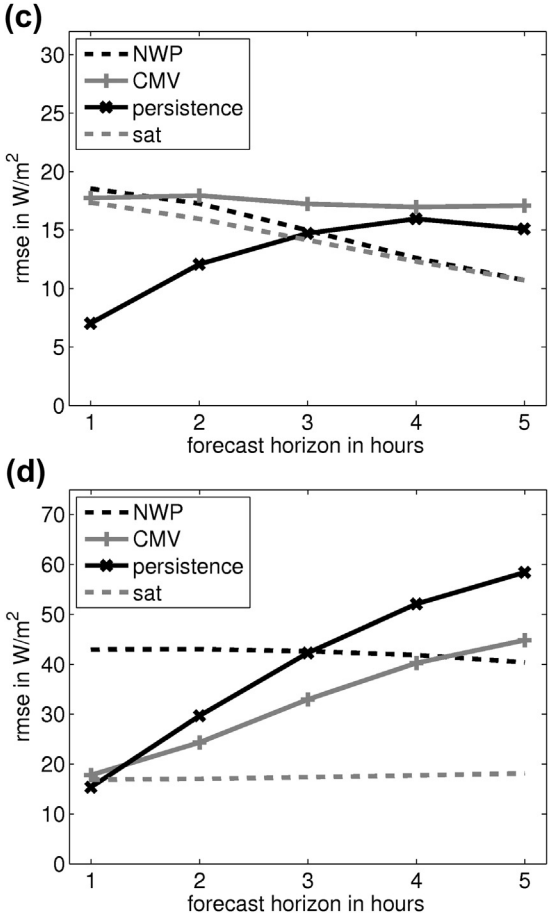

FIGURE 11.21 Continued.

components are obtained from GHI using empirical diffuse-fraction models that require information on solar geometry and atmospheric conditions. The direct radiation on the tilted plane can be derived from DNI by just considering the angle of incidence on the module plane. For modeling the diffuse plane-of-array radiation, more precise information on cloud conditions is necessary because the distribution of radiance across the sky hemisphere strongly differs for clear-sky, overcast, and broken-cloud situations. In addition, ground-reflected irradiance for tilted panels, which depends on ground reflectivity and module tilt, has to be considered. It usually contributes only a minor part to overall incident irradiance except for snow conditions, when ground reflectivity increases significantly (Lorenz & Heinemann, 2012).

The next step involves simulation of PV-system output as a function of plane-of-array global irradiance and module temperature, taking into account

differences in module type (crystalline silicon, amorphous silicon, or CIS), mounting technique (roof-mounted or free-standing), and inverter efficiencies. Following Beyer et al (Beyer et al., 2004), DC-power modeling requires module-specific information on irradiance and temperature dependency, which can be obtained from data-sheet information or measurements. Simulation of model efficiency is performed in two steps: first, the influence of irradiance deviating from standard test conditions (STC, referring to an incident irradiance of 1,000 W/m^2 at AM1.5 spectrum and a module temperature of 25°) is modeled considering different module types. Second, the performance at different module temperatures is modeled with respect to a module-specific temperature coefficient and an effective module temperature derived from ambient temperature and information on the mounting technique. The DC to AC conversion efficiency is considered in a last step, using a standard approach describing inverter efficiency as a function of DC input (Reich et al., 2011).

Detailed information on a PV system has to be available in order to simulate power output correctly. For regional power forecasts, these specifications usually are not available for all PV systems in the corresponding area. In any case, regional PV-power production can be estimated with sufficient accuracy by simulating the power output for a representative set of systems in the area. The predicted power output for the representative set is upscaled to regional forecasts of power production by linear extrapolation using the rated AC power. This approach reduces data-processing requirements and computational costs (Lorenz & Heinemann, 2012). Here, the representativeness of the subset of PV systems is crucial to regional-forecast quality. Most of it relates to the spatial distribution of the rated AC power of the installed PV systems. This information is available for Germany, since the grid code for the integration of renewable energies requires a registration of all PV systems with location and nominal power. Information on system orientation, tilt, and module type is also essential and has to be gathered from other sources (e.g. monitoring data). Evaluations of the described CMV method for irradiance forecasting and corresponding PV-power simulation will be one of the next steps in our research.

11.8. SUMMARY AND OUTLOOK

The demand for PV-power predictions, resulting from the increasing share of fluctuating PV power in the energy supply system, is rapidly growing. Forecasts on different timescales from a few hours to several days are required. The basis of PV-power prediction is forecasts of GHI, which can be derived from NWP models, satellite information, or ground measurements and through empirical or statistical methods. Here, we focused on irradiance predictions for the time horizon of several hours ahead, using CMVs derived from HRV images produced by MSG satellites. Consecutive images are compared to deduce information on current cloud motion, which is extrapolated to predict cloud conditions for the subsequent hours. CMV forecasts were evaluated using

irradiance measurements for a 1 y dataset (July 2011 through June 2012) comprising data from 274 stations distributed over Germany, and compared to ECMWF irradiance predictions and forecasts based on the assumption of persistence of the clear-sky index using irradiance measurements. It was shown that CMV forecasts outperform NWP forecasts up to 5 h ahead.

At 1 h ahead, CMV forecasts and persistence have a similar accuracy. For longer forecast horizons, CMV performs considerably better than persistence. Another focus of the evaluation was the assessment of regional-forecast accuracy in comparison to that of single sites. For regional aggregated irradiance over Germany, RMSE values are reduced to around one-third of the corresponding value for single sites. In addition to the overall evaluation, a detailed analysis of sensitivity to several parameters was performed. In particular, the accuracy of CMV forecasts based on visible-range image data strongly depends on Sun elevation at the time the forecasts are generated, showing poor results for elevations below 10°. This limits the time to which CMV forecasts are applicable and so early morning hours are not covered. This is especially a problem in winter months, when the Sun rarely reaches the required elevations. In summer months, when PV-power production is much greater than in other seasons, CMV forecasts outperform other forecasts for all forecast horizons up to 5 h. To allow for calculation of reliable CMV forecasts in the early morning, additional use of infrared satellite images for detecting clouds is a promising approach.

For improving accuracy in situations with forming or dissolving clouds or fog structures, which are not yet modeled by the cloud-motion detection algorithm, information from NWP forecasts such as low-level inversions or convective activity needs to be investigated.

Combining and integrating different forecasting methods into an optimized forecasting system covering all relevant time horizons and regional scales will be the focus of future research. In general, forecasts based on CMVs deliver good results for 4–5 h horizons. This complements other approaches based on NWP forecasts and real-time irradiance measurements for intraday or spot-market trading, respectively. Future developments may extend the hours these forecasts are available and improve horizon-dependent forecast accuracy.

REFERENCES

Bacher, P., Madsen, H., Nielsen, H.A., 2009 Online short-term solar power forecasting. Solar Energy 83 (10), 1772–1783.

Beyer, H.G., Constanco, C., Heinemann, D., 1996. Modifications of the Heliosat procedure for irradiance estimates from satellite data. Solar Energy 56, 121–207.

Beyer, H.G., Betcke, J., Drews, A., Heinemann, D., Lorenz, E., Heilscher, G., et al., 2004. Identification of a general model for the MPP performance of PV modules for the application in a procedure for the performance check of grid connected systems. In: 19th European Photovoltaic Solar Energy Conference and Exhibition. Paris, France, pp. 3073–3076.

Bofinger, S., Heilscher, G., 2006. Solar electricity forecast— Approaches and first results. In: 21st European Photovoltaic Solar Energy Conference. Dresden, Germany.

Bourges, B., 1992. Yearly variations of the Linke turbidity factor. Climatic data handbook of Europe, 61–64.

Cano, D., Monget, J.M., Albuisson, M., Guillard, H., Regas, N., Wald, L., 1986. A method for the determination of the global solar radiation from meteorological satellite data. Solar Energy 37 (1), 31–39.

Chow, C.W., Urquhart, B., Lave, M., Dominguez, A., Kleissl, J., Shields, J., et al., 2011. Intra-hour forecasting with a total sky imager at the UC3 San Diego solar energy testbed. Solar Energy 85 (11), 2881–2893.

Deutscher Wetterdienst, http://www.dwd.de/.

Dumortier, D., 1995. Modelling global and diffuse horizontal irradiances under cloudless skies with different turbidities. Tech. rep. 2. CNRS-ENTPE.

Engel, E., 2006. Kurzzeitvorhersage der solaren Einstrahlung -Potentiale der zweiten Generation von Meteosat-Satelliten. MA thesis. University of Oldenburg.

EUMETSAT, http://www.eumetsat.int/.

ECMWF, European Centre for Medium-Range Weather Forecasts, http://www.ecmwf.int/.

European Power Exchange, http://www.epexspot.com/en/.

Hammer, A., Heinemann, D., Lorenz, E., Lückehe, B., 1999. Short-term forecasting of solar radiation: a statistical approach using satellite data. Solar Energy, 1992, 67. pp. 139–150.

Hammer, A., Heinemann, D., Hoyer, C., Kuhlemann, R., Lorenz, E., Müller, R., et al., 2003. Solar energy assessment using remote sensing technologies. Remote Sensing of Environment 86 (3), 423–432.

Hammer, A., Lorenz, E., Petrak, S., 2007. Fernerkundung der Solarstrahlung fuer Anwendungen in der Energietechnik. In: Deutsch-österreichisch-schweizerische Meteorologentagung DACH.

Heinemann, D., Lorenz, E., Girodo, M., 2006. Forecasting of solar radiation. In: Dunlop, E.D., Wald, L., Suri, M. (Eds.), Solar Resource Management for Electricity Generation from Local Level to Global Scale. Nova Science Publishers, New York, pp. 83–94.

Schmetz, J., Pili, P., Tjemkes, S., Just, D., Kerkmann, J., Rota, S., et al., 2002. An Introduction to Meteosat Second Generation (MSG). Bulletin of the American Meteorological Society 83 (7), 977–992.

Klucher, T.M., 1979. Evaluation of models to predict insolation on tilted surfaces. In: Solar Energy 23, pp. 111–114.

Lorenz, E., Hurka, J., Heinemann, D., Beyer, H.G., 2009. Irradiance Forecasting for the Power Prediction of Grid-Connected Photovoltaic Systems. In: IEEE Journal of Selected Topics in Applied Earth Observations and Remote Sensing 2.1, pp. 2–10.

Lorenz, E., Heinemann, D., 2012. Prediction of Solar Irradiance and Photovoltaic Power. In: Comprehensive Renewable Energy. Elsevier, vol. 1, pp. 239–292.

Lorenz, E., Heinemann, D., Hammer, A., 2004. Short-term forecasting of solar radiation based on satellite data. EuroSun Conference Freiburg, Germany, 841–848.

Lorenz, E., Scheidsteger, T., Hurka, J., Heinemann, D., Kurz, C., 2010. Regional PV power prediction for improved grid integration. In: Progress in Photovoltaics: Research and Applications, Conference Proceedings, pp. 757–771.

Lorenz, E., Heinemann, D., Kurz, C., Nov. 2011. Local and regional photovoltaic power prediction for large scale grid integration: Assessment of a new algorithm for snow detection. In: Progress in Photovoltaics: Research and Applications.

Mathiesen, P., Kleissl, J., 2001. Evaluation of numerical weather prediction for intraday solar forecasting in the continental United States. Solar Energy 85 (5), 967–977.

Menzel, W.P., 2001. Cloud tracking with satellite imagery: From the pioneering work of Ted Fujita to the present. Bulletin of the American Meteorological Society 82 (1), 33–47.

Meteomedia GmbH. http://www.meteomedia.de/.

Perez, R., Ineichen, P., Moore, K., Kmiecik, M., Chain, C., George, R., Vignola, F., 2002. A new operational satellite-to-irradiance model. Solar Energy 73 (5), 307–317.

Perez, R., Kivalov, S., Schlemmer, J., Hemker Jr., K., Renné, D., Hoff, T.E., 2009. Validation of short and medium term operational solar radiation forecasts in the US. ASES Annual Conference, Buffalo.

Perez, R., Beauharnois, M., Hemker, K., Kivalov, S., Lorenz, E., Pelland, S., et al., 2011. Evaluation of Numerical Weather Prediction Solar Irradiance Forecasts in the US. In: Proc. ASES Ann. Conf. Raleigh, NC.

Reich, N.H., van Sark, W.H.J.H.M., Turkenburg, W.C., 2011. Charge yield potential of indoor-operated solar cells incorporated into product integrated photovoltaic (PIVP). Renewable Energy 36, 642–647.

Reikard, G., 2009. Predicting solar radiation at high resolutions: a comparison of time series forecasts. Solar Energy 83 (3), 342–349.

Remund, J., Schilter, C., Dierer, S., Stettler, S., Toggweiler, P., 2008. Operational forecast of PV production. In: 23rd European Photovoltaic Solar Energy Conference. Valencia, Spain.

Wirth, H., 2013. Aktuelle Fakten zur Photovoltaik in Deutschland. Tech. rep. Fraunhofer ISE, Freiburg, Germany.